Lithuanian Journal of Physics
Vol. **63**, No. 3, pp. 113–121 (2023)
ISSN 1648-8504 eISSN 2424-3647
DOI: https://doi.org/10.3952/physics.2023.63.3.1

ON EVALUATION OF IMAGE QUALITY IN NONPARAXIAL SINGLE-PIXEL IMAGING

K. Mundrys [a], S. Orlov [a], P. Kizevičius [a], L. Minkevičius [b], and G. Valušis [b]

[a] *Department of Fundamental Research, Center for Physical Sciences and Technology, Saulėtekio 3, 10257 Vilnius, Lithuania*
[b] *Department of Optoelectronics, Center for Physical Sciences and Technology, Saulėtekio 3, 10257 Vilnius, Lithuania*
Email: sergejus.orlovas@ftmc.lt

Received 22 March 2023; revised 16 May 2023; accepted 22 May 2023

High numerical apertures lead to an appearance of distortions in a single-shot image, which make obtaining images troublesome if not impossible. These obstacles can be overcome in single-pixel imaging, where different strategies lead to inspection of objects with a good resolution, contrast and brightness. Recent advances in flat photonic elements have enabled the creation of compact nonparaxial imaging systems, which are especially promising in the THz range of wavelengths, bringing advances to such fields as communication, material inspection and spectroscopy. In this work, we dive into the problematics of single-pixel imaging: we introduce an object sample, which we use to investigate the resolution, contrast and brightness of the classical two-lens imaging setup. We evaluate the nonparaxial imaging of the sample and report that the conditions for the best contrast and the best brightness are decoupled in nonparaxial single pixel imaging. To overcome this hurdle, we use two integral image quality assessment techniques from computational imaging theory and estimate the quality of the image in a virtual numerical THz imaging scenario. The localized mean square error metric did not cause additional constraints to the quality of the image, whereas the global mean square error has restricted the range of possible imaging setups. Thus, the computational integral image quality assessment techniques back up the main claim of this study that in the single-pixel imaging the resolution is decoupled from the image brightness.

Keywords: nonparaxial imaging, single-pixel imaging, contrast, resolution, image quality assessment

1. Introduction

Image retrieval is a long-standing research area that began with the invention of cameras. Today, images are usually retrieved by using a camera lens to form an image and a detector array to record it. Due to the fast progress of CMOS and CCD technologies driven by global market needs, digital cameras and cellphones can capture images with millions of pixels using a very small chip. The number of pixels in a camera sensor has already exceeded 20 million, which seems unnecessary and wasteful for data storage in normal applications. Instead, an image can be reconstructed with a single-pixel detector by measuring how much a scene overlaps with different masks using a single element detector [1] and then combining the measurements with the mask information [2]. This technique is validated theoretically [3], experimentally [4] and has been extended even to the 3D reconstruction of objects [5, 6]. This imaging technique goes back more than 100 years, when scientists and inventors tried to retrieve images using a single-pixel detector, such as an 'electric telescope' with a spiral perforated disk by Nipkow in 1884 [7] and the 'televisor' by Baird in 1929 [8]. This was called a raster scan and its mathematical theory was developed in 1934 [9]. Raster scan systems are still used for nonvisible spectra, where detector arrays of some wavelengths are too costly or unavailable.

In recent years, ghost imaging has revived research interest in single-pixel imaging architectures after its first experimental demonstration [1, 2]. However, ghost imaging is sometimes called a computational imaging technique, where 'computational' means that the imaging data measured by a ghost imaging system need to be processed by computational algorithms to look like a normal

image [3, 4, 6]. Using a single-pixel detector in imaging hardware may have advantages over a pixelated detector array in terms of detection efficiency, noise reduction and time resolution, but computational algorithms also bring benefits from the software perspective, due to increased processing power [3]. Both the single-pixel imaging community and the ghost imaging community soon realized that the two imaging architectures are essentially the same optically. Single-pixel imaging uses a spatial light modulator (SLM) on the focal plane of the camera lens to modulate the image of the scene with different masks before measuring the light intensities with a single-pixel detector, while ghost imaging uses different structured light distributions created by the SLM to illuminate the scene and measure the reflected or transmitted light intensities [4–6].

Structured electromagnetic fields have many applications in areas such as communication, metrology and light–matter interactions [10]. Most of the progress is due to the fast development of non-diffracting electromagnetic beams that can be used for a wide range of wavelengths, from the visible to the THz range [11]. These beams have interesting properties, such as resistance to diffraction and dispersion, self-healing, self-acceleration, etc. The usefulness of nondiffracting beams can be greatly enhanced when their vortical and polarization properties are added [12]. These unconventional light states can also be used to improve imaging [13], where high resolution is very important, and is usually achieved with Gaussian illumination in high numerical aperture systems. However, the structured illumination has recently been used successfully for these imaging improvements in the THz region using laser-fabricated flat optics [14].

This work was motivated by recent developments in single-pixel raster scan imaging [14], where different imaging setups with structured illumination were extensively benchmarked using a non-transparent sample with 12 groups of lines of different widths. The main drawback of this approach is that the number of groups is small, which makes it difficult, if not impossible, to observe any fine differences between setups involving different schemes. Here, we describe a method that uses a sample with fine-tuned line widths, enabling one to determine the resolution with a high accuracy. We test the sample by performing a numerical experimentation of nonparaxial imaging involving a classical setup using only two lenses and discuss such physical values like contrast and resolution. While doing so, we encounter a new finding – in the nonparaxial single-pixel imaging, unlike in the single-shot imaging, the best resolution is independent of the best image brightness. These findings raise the question of whether physical metrics give valid results. Further in the work, we use image quality assessment metrics which are used in computational imaging to determine the actual performance of the imaging system. We reveal that the image quality assessment is also not as straightforward as expected in the nonparaxial single-pixel imaging. High resolution can still be achieved in regions where the brightness of the image is low. These tests of the imaging sample raise important questions and require further investigation, both numerically and experimentally.

2. Theoretical background

The typical THz wavelengths λ are rather long (in our simulations λ = 0.5 mm, or the frequency of 0.6 THz); thus, photonic elements with typical sizes of a few centimetres are nonparaxial objects. Our main aim is to test a new toy sample to determine the resolution with a high fidelity. As we are not interested here in the performance of the nonconventional imaging systems, previously reported elsewhere [13, 14], we provide focusing and imaging abilities using a conventional lense with the phase $\Phi(\mathbf{r})$ of the transmission function $T(\mathbf{r}) = \exp(\mathrm{i}\Phi(\mathbf{r}))$ being a quadratic function

$$\Phi(\mathbf{r}) = \frac{k}{2f}(x^2 + y^2), \tag{1}$$

where f = 1 cm is the expected paraxial focus length.

We start the discussion by recalling the nonparaxial Rayleigh–Sommerfeld diffraction integral [15]

$$U_1(\mathbf{r}_1) = \frac{1}{\mathrm{i}\lambda} \times \int_{S_A} U_{\mathrm{inc}}(\mathbf{r}_0) T(\mathbf{r}_0) \frac{\exp[\mathrm{i}k\,|\,\mathbf{r}_{01}\,|]}{|\,\mathbf{r}_{01}\,|} \cos(\mathbf{r}_{01}, \mathbf{n})\mathrm{d}S, \tag{2}$$

where $U_1(\mathbf{r}_1)$ is the field in the observation plane, $U_{\mathrm{inc}}(\mathbf{r}_0)$ is the incident field in the diffraction plane, and $T(\mathbf{r}_0)$ is the transmittance of the object. The coordinates of the observation plane are $\mathbf{r}_0 = (x_0, y_0,$

$z = 0$) and the coordinates of the observation plane are $\mathbf{r}_1 = (x_1, y_1, z = z_1)$, the vector $\mathbf{r}_{01}$ is the distance between two points in these planes, and $\mathbf{n}$ is normal to the surface of the object. Integration is performed on the surface of element S_A. On the basis of this consideration, we have employed a propagator using spherical point sources to numerically model the propagation of the electromagnetic field within the system.

The numerical experiment is performed as follows. First, Eq. (2) is applied to propagate the electromagnetic field of the incident radiation from the first lense to the sample (see Fig. 1). Next, the resulting field $U_1(\mathbf{r}_1)$ is multiplied with the object transmission function $T_{obj}(\mathbf{r}_1)$ and the field is propagated to the second lense (see Fig. 1),

$$U_2(\mathbf{r}_2) = \frac{1}{\mathrm{i}\lambda} \times \int_{S_A} U_i(\mathbf{r}_1) T_{obj}(\mathbf{r}_1) \frac{\exp[\mathrm{i}k\,|\,\mathbf{r}_{12}\,|]}{|\,\mathbf{r}_{12}\,|} \cos(\mathbf{r}_{12}, \mathbf{n}) \mathrm{d}S, \quad (3)$$

where the coordinates $\mathbf{r}_2 = (x_2, y_2, z = z_2)$ are of the plane of the second lense. The vector $\mathbf{r}_{12}$ is the distance between two points in these planes, and $\mathbf{n}$ is normal to the surface of the sample.

Lastly, the electromagnetic field $U_2(\mathbf{r}_2)$ multiplies with the transmission function of the second lense and propagates to the single-pixel detector, located at $\mathbf{r}_3 = (x_3 = 0, y_3 = 0, z = z_3)$:

$$U_3(\mathbf{r}_3) = \frac{1}{\mathrm{i}\lambda} \times \int_{S_A} U_2(\mathbf{r}_2) T(\mathbf{r}_2) \frac{\exp[\mathrm{i}k\,|\,\mathbf{r}_{23}\,|]}{|\,\mathbf{r}_{23}\,|} \cos(\mathbf{r}_{23}, \mathbf{n}) \mathrm{d}S. \quad (4)$$

This operation is consecutively performed for different positions of the sample, which is raster-scanned in the x_2 and y_2 directions. This is the theoretical basis for our further numerical experimentation.

3. Dissection of numerical experiments using a selection of metrics

The selection of the imaging sample was motivated by our recent research (see Ref. [14]). In that work, the resolution was determined using a sample containing 12 groups of four lines with different line widths. Due to the limited number of such groups, the resolution could not be determined very finely – the sample could provide only 12 different linewidths per mm. In order to solve this, we have prepared a similar sample, containing groups of four lines with varying line widths (see Fig. 2). As the number

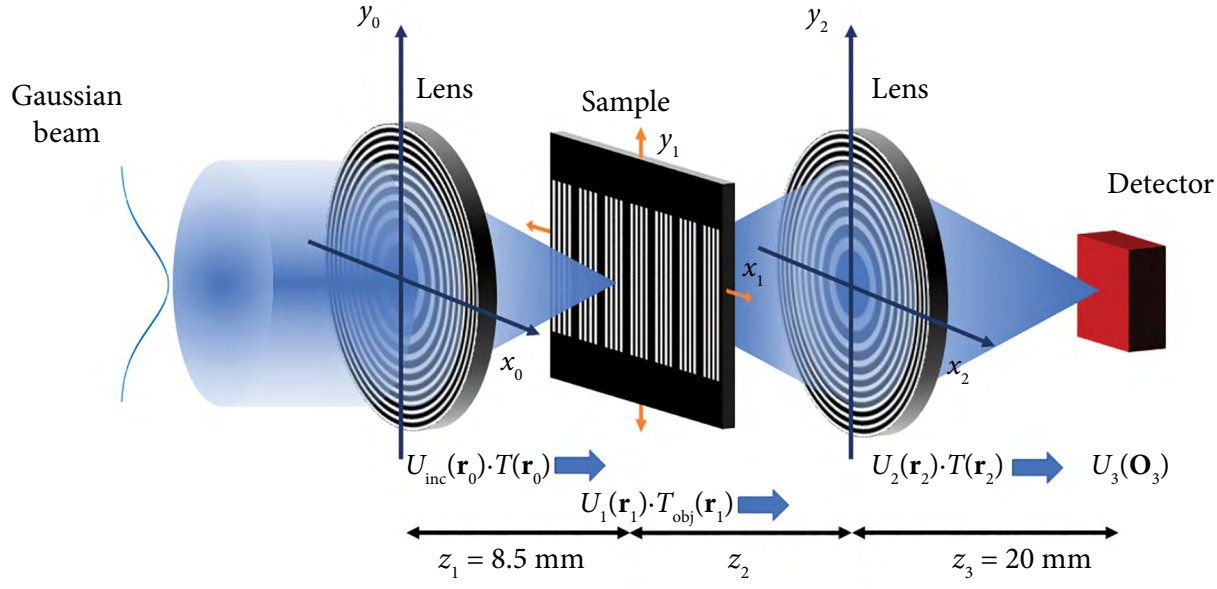

Fig. 1. A schematic representation of the setup for numerical experimentation. The spherical wave propagator is successively applied three times: (i) to calculate the propagation from the plane (x_0, y_0) to the plane of the object (x_1, y_1), (ii) to calculate the propagation from the plane (x_1, y_1) to the plane of the object (x_2, y_2), and (iii) to calculate the propagation from the plane (x_2, y_2) to the single-pixel detector $(x_1, y_1) = (0, 0)$. The Detector is a single-pixel camera. The sample is scanned by raster in the x_1 and y_1 directions (orange arrows).

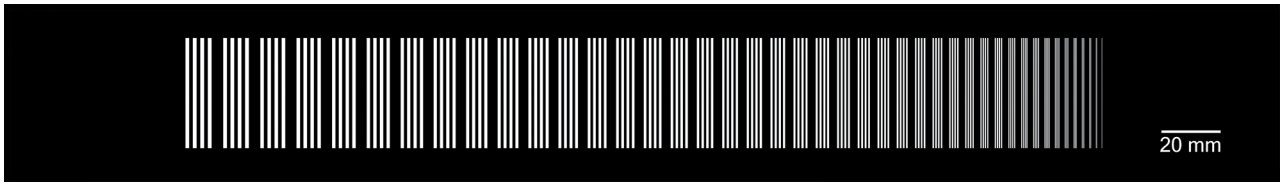

Fig. 2. A sample of the object used to determine the parameters of the image. The sample contains equidistant groups of four lines. The width of the lines decreases from left to right. The scale bar is only for size estimates. The number of pixels in the sample in the x direction is 14,710, the size of a single pixel is 29.297 μm.

of groups with different lines is significantly larger than twelve, the resolution can be determined with a higher accuracy than in the previous work.

Although resolution is commonly believed to be a space dimension, this description does not provide a complete understanding [16]. In reality, resolution can be more accurately defined as a spatial frequency measured in line pairs per millimetre (lin/mm). A line pair comprises a duo of adjacent black and white stripes in the object space, and whether the stripes can be seen as separate entities at a given resolution is contingent on a grayscale level. The contrast, or grayscale difference, between the squares and the space between them is crucial to determine how easily a system can resolve a line pair. Consequently, the resolution is defined as a spatial frequency, given in lin/mm, at which a specific contrast is attained (see more in Ref. [16]). Although contrast is generally established by convention by different lens and camera manufacturers, lenses are generally specified to have a contrast of 20%. Therefore, determining the resolution in terms of lin/mm is highly advantageous for comparing lenses and selecting the best one for a given application and sensor [16, 17].

Contrast plays a critical role in defining resolution, as it determines how well black and white details can be distinguished at a given frequency. An image appears well-defined when black details appear black and white details appear white, and as black and white information trends into intermediate grays, the contrast at that spatial frequency decreases. A greater intensity difference between light and dark line results in a better contrast, which is essential for producing high-quality images.

To calculate the contrast at a spatial given frequency, the maximum intensity $I_{\max}$ is introduced, and $I_{\min}$ represents the minimum intensity:

$$\text{Contrast} = \left[\frac{I_{\max} - I_{\min}}{I_{\max} + I_{\min}}\right] \times 100\%. \qquad (5)$$

Here, it is important to stress that the concept of contrast can be applied to both the object and its image. The resulting contrast is defined as the percentage of contrast of the object reproduced in the image space, assuming no loss of contrast from illumination (plane wave illumination). The illumination, in general, might have its own non-homogeneous pattern which through the illumination of the object might affect the contrast of the image in a negative way. However, the perfect reproduction of object contrast and resolution is not possible due to the diffraction and further physical limitations of optical systems. Even a perfectly designed and manufactured lens system cannot fully reproduce the resolution and contrast of an object due to the nature of light [16, 17].

With this in mind, we proceed now to numerical simulations in the following setup (see Fig. 1). This is a general setup, largely mimicking the experimental setup from Ref. [14]. The sample is placed at the distance z_1 from element 1, which is a lens with the square-phase transmission function (see Eq. (1)). Due to nonparaxiality, the brightest illuminating spot is not formed at 1 cm, but at the distance z_1 = 8.5 mm. We use this distance in more detail throughout the manuscript. In the single-shot imaging, the fixed distance between the detector and the collecting lense results in the single best distance between the object and the collecting lense. Our aim here is to prove this by varying the second distance z_2 – the distance between the object and the collecting lense.

We did a raster scan of the sample in the x direction for various constant y positions and did not find significant differences unless the value y is chosen so that we are at the corner of the visually loaded area. For this reason, we fix now our efforts on the raster scanning of the central part of the object. A comparison of the image obtained using single-pixel imaging for one particular distance is given in Fig. 3.

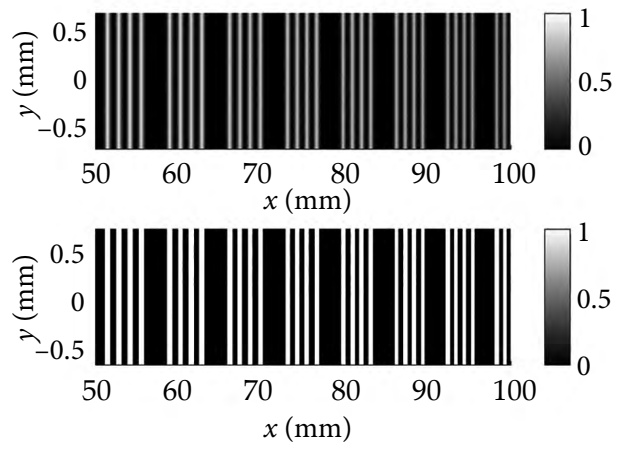

Fig. 3. A comparison of the particular part of the single-pixel image (top) and the object (bottom). The sample was scanned as a raster in the x and y directions.

This is a basic example of the images that we obtain for the fixed distance z_2. We note the homogeneity of the picture in the y direction as a further indication of the right choice that we made for further consideration. As we see from Fig. 3, the contrast of the object is high and not affected by the illumination. The resulting contrast of the image is affected by the propagation through the collecting lense and by the single-pixel detector.

The resolution is specified at a particular contrast level (see Fig. 4(a)). In the paraxial imaging, the perfect reproduction of the object, including sharp transitions at the edge of the pixel, is assumed, but this is never fully achieved in practice (see Fig. 4(b–d)). Even a well-designed and manufactured lens cannot completely reproduce an object

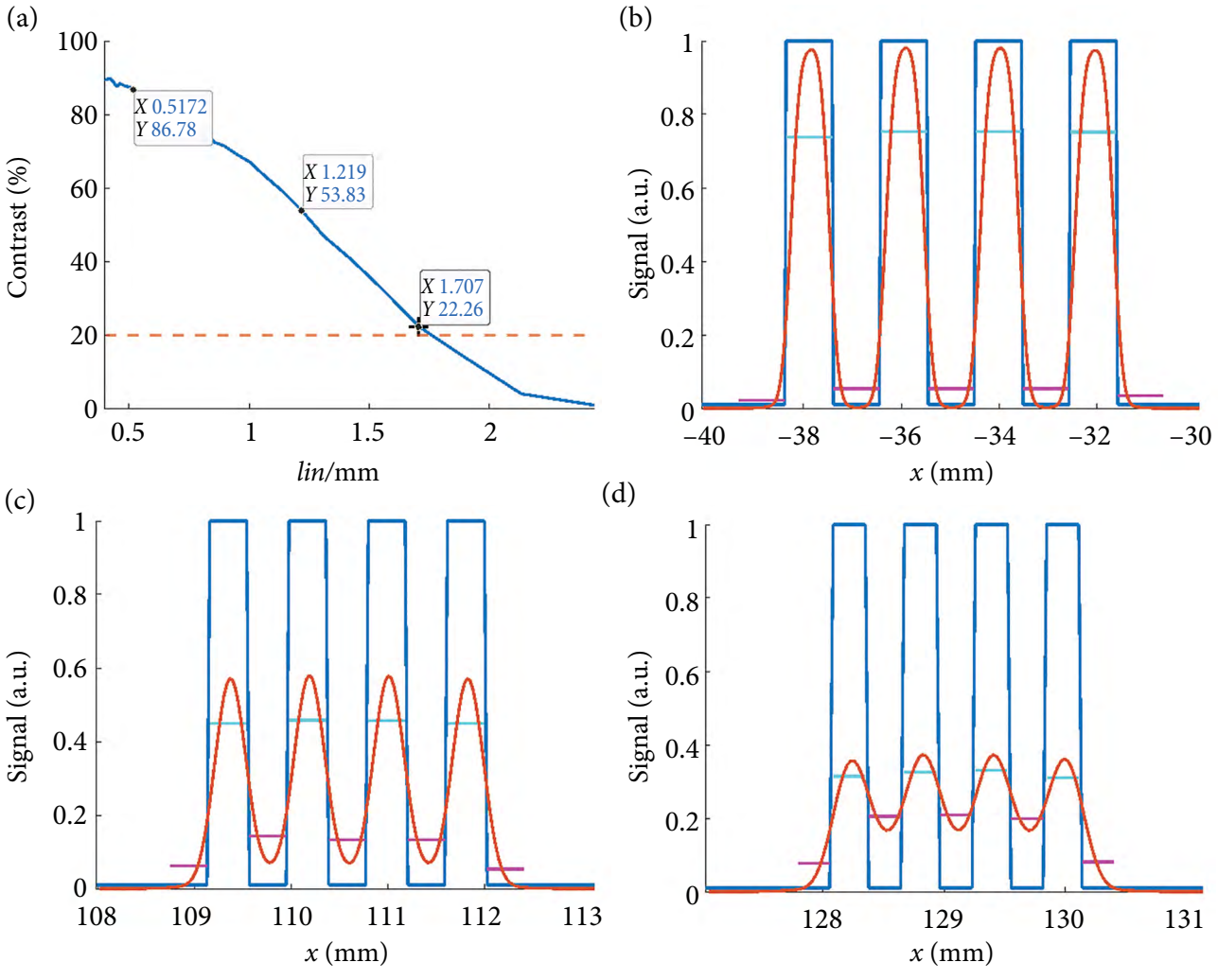

Fig. 4. An example of determining the resolution of the imaging system using the definition of contrast. (a) Dependence of the numerically estimated contrast on the number of lines per millimetre. The red line represents the level of 20%. Three points are present in the curve, and a comparison of the sample and the signal is given in (b–d). The green lines are averages of the maximal value of the signal, and the pink lines are averages of the minimal value of the signal in the corresponding regions of the sample.

resolution and contrast due to the nature of light (see Fig. 4(a)). The resolving power of the system depends on its ability to detect the space between objects. As the lines approach each other, the blurs overlap and the system resolving power is reduced (see Fig. 4(c)) and becomes below the acceptable level (see Fig. 4(d)). The laboratory achievable resolution is additionally influenced by other various factors, including the blur caused by alignment and optical errors, nonideal object detail spacing and the sensor ability to detect the contrast at the relevant detail size.

The contrast function, which we show in Fig. 4(a), is also called within computational imaging the modulation transfer function [16]. The point where the modulation function line and the line representing the system sensor's minimum detectable modulation intersect determines the system's limiting resolution (see Fig. 4(a)). The threshold curve that indicates the minimum detectable modulation for a system or sensor, also known as an AIM curve (aerial image modulation), describes the response characteristics of such systems as an eye, films, image tubes, CCDs, and other devices. It is important to note that the modulation threshold typically increases with spatial frequency, although there are some exceptions [16]. For convenience, we set it as a constant at the 20% level.

As a next step, in our discussion, we represent the sample for the different positions of the collecting lens z_2 as a single object (see Fig. 5). This image

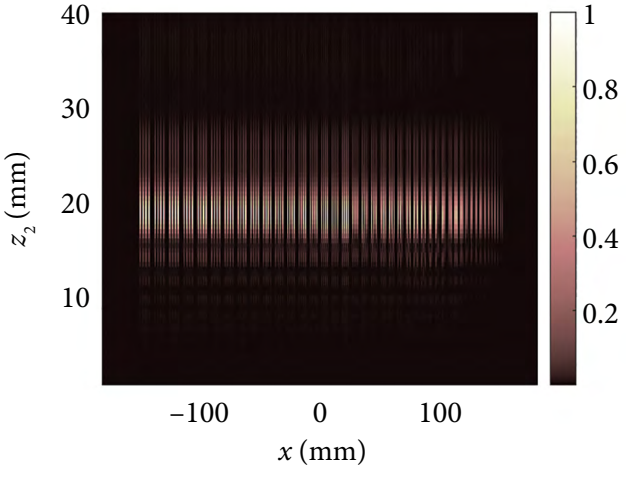

Fig. 5. A representation of the sample for the different positions of the collecting lens z_2. The picture was obtained by combining the central x cuts of the sample for different configurations.

was obtained using a combination of cuts from the central sample for different distances z_2 while maintaining the intensity information. The main problem with the definition of contrast in Eq. (5) is that it loses information such as intensity. Thus, theoretically, we may find a situation where distances z_2 ensure the best contrast and resolution, but the intensity is low in that region, which potentially harms object inspection. Indeed, as we might note from Fig. 5, there is a region of distances from the object to the lense, where the intensity is highest.

To overcome this hurdle, we look at image quality assessment techniques from the computational imaging. Numerous techniques are available to assess the quality of images, such as MSE (mean square error), UIQI (universal image quality index), PSNR (peak signal-to-noise ratio), SSIM (structured similarity index method), HVS (human vision system) and FSIM (feature similarity index method) [18]. We select the mean square error between the image and the object as a second metric for image inspection. This metric is the most known and popular in image quality assessment [19] and is defined as

$$\mathrm{MSE} = -\frac{1}{N}\sum_{i=1}^{N} |\, Object_i - Image_i \,|^2, \qquad (6)$$

where the summation index i is the pixel number either in the representation of the *Object* or of the *Image* (see Fig. 3) and N is the total number of pixels. Note the minus sign, which was introduced to enhance the visual comparison between the methods. MSE, as defined in Eq. (6), is the most commonly used estimator of image quality measurement and is a full reference metric where values closer to zero indicate a better quality. MSE measures the second moment of the error between the *Object* and the *Image* and incorporates both the variance and bias of the estimator. The estimator is the procedure used to measure an unobserved quantity of the image [18, 19]. The MSE represents the variance of the estimator when it is unbiased and has the same units of measurement as the quantity being calculated, such as the variance. The MSE calculates the average of the squared errors, which is the difference between the estimator and the estimated result.

Whereas the contrast calculation is local and depends on the number of pixels, the MSE estimates

the average of the line group in the imaged sample, so it is also useful to introduce an alternative metric, the local MSE

$$\mathrm{MSE} = -\frac{1}{N}\sum_{i=1}^{N}\left|Object_i - \frac{Image_i}{\max Image}\right|^2, \qquad (7)$$

where the image is normalized to unity by division with the maximum value of the line group max *Image*. This metric is useful, as it should counteract situations when the locality of the contrast determination might not determine the quality of the image.

As expected, the contrast map in Fig. 6(a) reveals numerous distances z_2, where the sample is resolved with a high resolution. Some discrepancies are also observed; one may note areas with suddenly appearing high-contrast regions, which may falsely occur locally due to the locality of the algorithm. This might seem to contradict the common sense, since in single-shot imaging a good resolution is possible only at a single distance z_2 where the image brightness is also the best.

The metric from the computational imaging – the normalized MSE – in Fig. 6(b) supports this result, as it largely follows the trends of the contrast map compared to Fig. 6(a). Although in some areas with a high contrast, we observed higher than expected MSE values. This is a new result for the theory of imaging, as both diferential metric (contrast) and integral metric (MSE) demonstrate similar results, indicating that in the nonparaxial single-pixel imaging the best contrast position is less restricted than in the single-shot imaging.

The assumingly contradictory riddle of the nonparaxial single-pixel imaging is solved in Fig. 6(c), where we plot the brightness of the recorded image. The image is brightest at the single distance

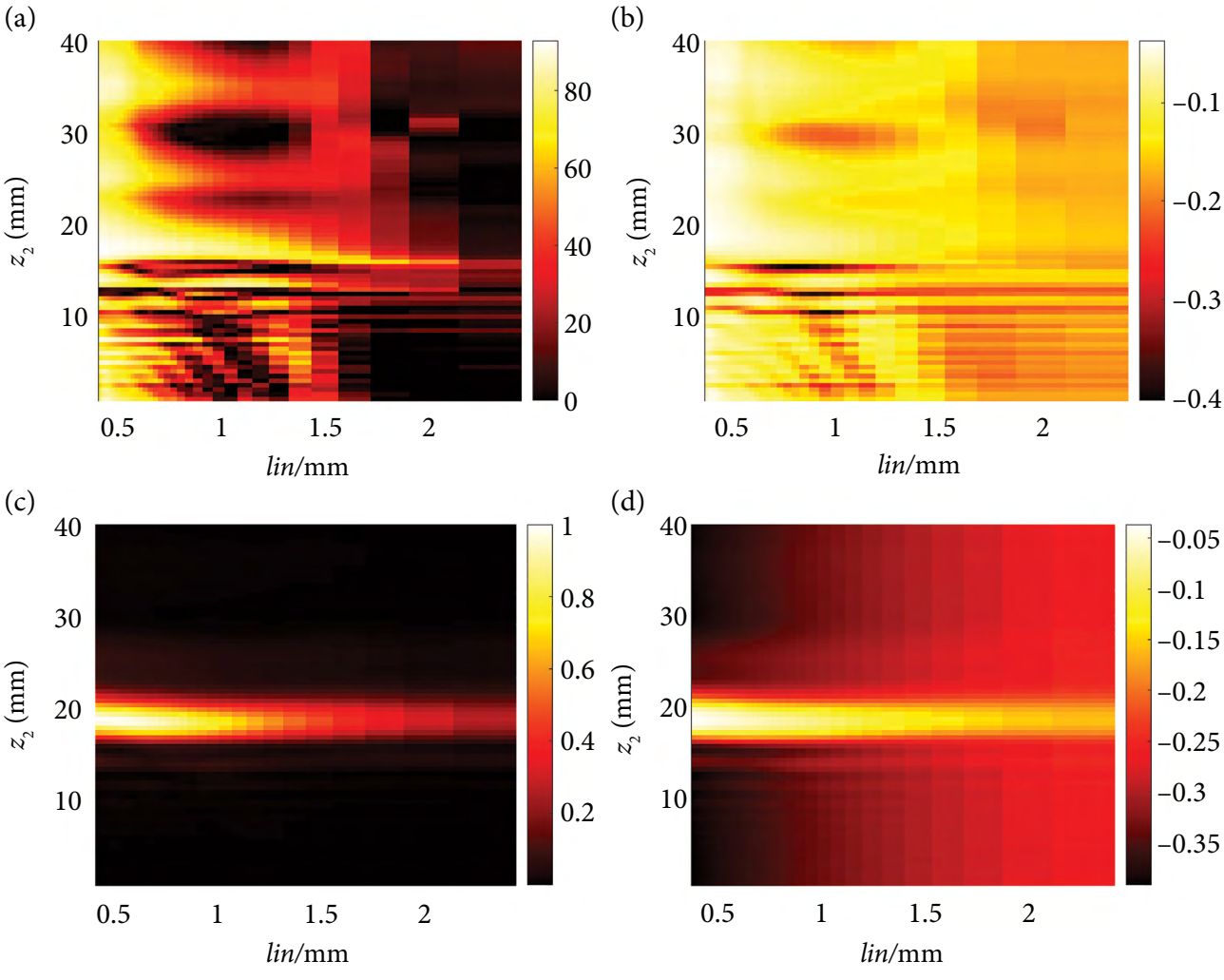

Fig. 6. Dependence of various image quality metrics on the position of the imaging lense z_2 and the line width in millimetres for contrast (a), normalized mean square error (b), image brightness (c) and mean square error (d).

$z_2 \approx 19.5$ mm, which is more or less in line with expectations from the single-shot imaging theory. The standard integral metric (MSE) is presented in Fig. 6(d) and, as we note, it is basically an overlap of the contrast and brightness maps from Fig. 6(a, c). This is especially noticeable by the appearance of high MSE values in regions with a low overall image brightness.

Our initial quest to introduce a toy sample for the fine determination of the resolving power of an optical system in nonparaxial single-pixel imaging has resulted not in the determined answers but in even more new questions, which have to be investigated. First of all, the results indicate that the condition for the best contrast decouples, i.e. becomes independent from the condition for the best image brightness. This makes the assessment of the image quality in the single-pixel image not as straightforward as in the single-shot imaging, where the best resolution and the best brightness are observed.

In conclusion, we have presented a toy model for single-pixel imaging in the nonparaxial regime, which enables us to determine the resolution of the imaging system with a high fidelity. It turns out that image quality assessment is not as straightforward in nonparaxial single-pixel imaging as it is in single-shot imaging. The evaluation back up by diffraction theory has revealed that the best contrast and the best image brightness are decoupled in the nonparaxial single-pixel imaging. To verify this claim, we have performed image quality assessment benchmarks using two different integral computational metrics: mean square error and normalized mean square error. These benchmarks from computational imaging theory somehow restrained the conditions obtained from the physical theory, but it seems that the conditions for a good resolution and contrast are still independent from the conditions for a good image brightness. This study raises the question whether these findings can be transferred to alternative imaging setups, like those already present in the literature [13, 14]. Further numerical and experimental studies on this topic are undergoing and will be presented elsewhere.

Acknowledgements

This research has received funding from the Research Council of Lithuania (LMTLT), Agreement No. [S-MIP-23-71]. The authors acknowledge the support of colleagues from the Coherent Optics Laboratory throughout the discussions.

References

[1] T.B. Pittman, Y. Shih, D. Strekalov, and A.V. Sergienko, Optical imaging by means of two-photon quantum entanglement, Phys. Rev. A **52**, R3429 (1995).

[2] J.H. Shapiro, Computational ghost imaging, Phys. Rev. A **78**, 061802 (2008).

[3] M.F. Duarte, M.A. Davenport, D. Takhar, J.N. Laska, T. Sun, K.F. Kelly, and R.G. Baraniuk, Single-pixel imaging via compressive sampling, IEEE Signal Process. Mag. **25**, 83 (2008).

[4] M.P. Edgar, G.M. Gibson, and M.J. Padgett, Principles and prospects for single-pixel imaging, Nat. Photonics **13**, 13 (2019).

[5] M.-J. Sun and J.-M. Zhang, Single-pixel imaging and its application in three-dimensional reconstruction: a brief review, Sensors **19**, 732 (2019).

[6] C.A. Osorio Quero, D. Durini, J. Rangel-Magdaleno, and J. Martinez-Carranza, Single-pixel imaging: An overview of different methods to be used for 3D space reconstruction in harsh environments, Rev. Sci. Instrum. **92**, 111501 (2021).

[7] R.F. Lyon, in: *Digital Photography II*, Vol. 6069 (SPIE, 2006) p. 606901.

[8] B.J. Logie, *Apparatus for Transmitting Views or Images to a Distance*, US Patent 1,699,270 (1929).

[9] P. Mertz and F. Gray, A theory of scanning and its relation to the characteristics of the transmitted signal in telephotography and television, Bell Syst. Tech. J. **13**, 464 (1934).

[10] H. Rubinsztein-Dunlop, A. Forbes, M.V. Berry, M.R. Dennis, D.L. Andrews, M. Mansuripur, C. Denz, C. Alpmann, P. Banzer, T. Bauer, et al., Roadmap on structured light, J. Opt. **19**, 013001 (2016).

[11] M. Mazilu, D.J. Stevenson, F. Gunn-Moore, and K. Dholakia, Light beats the spread: "non-diffracting" beams, Laser Photonics Rev. **4**, 529 (2010).

[12] Y. Shen, X. Wang, Z. Xie, C. Min, X. Fu, Q. Liu, M. Gong, and X. Yuan, Optical vortices 30 years on: OAM manipulation from topological charge

to multiple singularities, Light Sci. Appl. **8**, 90 (2019).

[13] L. Minkevičius, D. Jokubauskis, I. Kašalynas, S. Orlov, A. Urbas, and G. Valušis, Bessel terahertz imaging with enhanced contrast realized by silicon multi-phase diffractive optics, Opt. Express **27**, 36358 (2019).

[14] R. Ivaškevičiūtė-Povilauskienė, P. Kizevičius, E. Nacius, D. Jokubauskis, K. Ikamas, A. Lisauskas, N. Alexeeva, I. Matulaitienė, V. Jukna, S. Orlov, et al., Terahertz structured light: nonparaxial Airy imaging using silicon diffractive optics, Light Sci. Appl. **11**, 326 (2022).

[15] M. Born and E. Wolf, *Principles of Optics: Electromagnetic Theory of Propagation, Interference and Diffraction of Light* (Elsevier, 2013).

[16] W.J. Smith, *Modern Optical Engineering: The Design of Optical Systems* (McGraw-Hill Education, 2008).

[17] E.H. Stelzer, Contrast, resolution, pixelation, dynamic range and signal-to-noise ratio: fundamental limits to resolution in fluorescence light microscopy, J. Microsc. **189**, 15 (1998).

[18] U. Sara, M. Akter, and M.S. Uddin, Image quality assessment through FSIM, SSIM, MSE and PSNR – a comparative study, J. Comput. Commun. **7**, 8 (2019).

[19] Z. Wang, A.C. Bovik, H.R. Sheikh, and E.P. Simoncelli, Image quality assessment: from error visibility to structural similarity, IEEE Trans. Image Process. **13**, 600 (2004).

DĖL VAIZDO KOKYBĖS ĮVERTINIMO NEPARAKSIALINIAME VIENO PIKSELIO VAIZDINIME

K. Mundrys [a], S. Orlov [a], P. Kizevičius [a], L. Minkevičius [b], G. Valušis [b]

[a] *Fizinių ir technologijos mokslų centro Fundamentinių tyrimų skyrius, Vilnius, Lietuva*

[b] *Fizinių ir technologijos mokslų centro Optoelektronikos skyrius, Vilnius, Lietuva*

Santrauka

Esant didelei skaitmeninei apertūrai, vieno kadro vaizdinime atsiranda iškraipymų, dėl kurių kokybiškus vaizdus gauti yra sunku, o kartais gal net neįmanoma. Šias kliūtis galima įveikti naudojant vieno pikselio vaizdinimą, kai įvairios strategijos leidžia matyti objektus, pasižyminčius gera skiriamąja geba, kontrastu ir ryškumu. Naujausi plokščiosios fotonikos pasiekimai leido sukurti kompaktiškas neparaksialines vaizdinimo sistemas, kurios yra ypač perspektyvios THz bangų ilgių diapazone bei yra pažangios tokiose srityse kaip komunikacija, medžiagų tikrinimas bei spektroskopija. Šiame darbe nagrinėjama vieno pikselio vaizdinimo problematika: pristatomas bandinio pavyzdys, kuris naudojamas dviejų zoninių plokštelių vaizdinimo sistemos skyrai, kontrastui ir ryškumui nustatyti. Atliekamas neparaksialinis bandinio vaizdinimas ir parodoma, kad geriausio kontrasto ir geriausio ryškio sąlygos yra viena nuo kitos atsietos neparaksialiniame vieno pikselio vaizdinime. Tikintis apeiti šią netikėtą kliūtį, pasinaudota dviem integraliais vaizdo kokybės vertinimo metodais iš skaitmeninių vaizdų teorijos ir jais remiantis įvertinta vaizdo kokybė virtualiame skaitmeniniame THz vaizdinimo scenarijuje. Lokalizuoto vidutinio kvadratinio nuokrypio metrika papildomai neapriboja gero vaizdo kokybės sąlygų, o suminis vidutinis kvadratinis nuokrypis stipriai apriboja galimų vaizdinimo atstumų diapazoną. Taigi, skaitmeniniai integralūs vaizdo kokybės nustatymo metodai patvirtina pagrindinį šio tyrimo teiginį, kad vieno pikselio vaizdo skiriamoji geba yra atsieta nuo vaizdo ryškumo.